25th ABCM International Congress of Mechanical Engineering
October 20-25, 2019, Uberlândia, MG, Brazil

COBEM2019-2410
MICROSTRUCTURE, MECHANICAL PROPERTIES AND CORROSION SUSCEPTIBILITY OF Ti-35Nb-4Sn ALLOY PROCESSED BY LASER MELTING

Juliane Ribeiro da Cruz
Mechanical Engineering Department, Aeronautics Institute of Technology (ITA), Praça Marechal Eduardo Gomes, 50, 12228-900, São José dos Campos, Sao Paulo, Brazil
juliane.rcruz@gmail.com

Milton Sérgio Fernandes de Lima
Institute of Advanced Studies (IEAv), Photonics Division, Trevo Cel Av José Alberto Albano do Amarante, 01, São José dos Campos, SP 12228-001, Brazil
miltonsflima@gmail.com

Rodnei Bertazzoli
Faculty of Mechanical Engineering, State University of Campinas, Mendeleyev, 200, 13083-860, Campinas, São Paulo, Brazil
rbertazzoli@fem.unicamp.br

Abstract. *The effect of laser melting on the corrosion susceptibility and mechanical properties of Ti-35Nb-4Sn (mass%) alloy is investigated across the melted track profile. Microstructure is assessed by optical and scanning electron microscopy, and by energy dispersive x-ray spectroscopy. Mechanical properties are determined by Vickers microhardness measurements and by nanoindentation analysis. Corrosion susceptibility is investigated by linear potential scan voltammetry. In comparison to the cold-rolled microstructure of base metal, plastic energy absorption and pitting corrosion resistance were improved in heat affected zone (HAZ) due to recrystallization and eventual reduction of active sites for pit nucleation. In fusion zone, however, passivation was compromised by the formation of dendritic microstructure with Sn enriched interdendritic region, where preferential pitting corrosion occurred. Fusion zone was the most anodic region and presented a corrosion potential difference of 35mV, in comparison to the adjacent and most cathodic HAZ. Local increase in elastic modulus and microhardness of fusion zone shows that laser melting is a viable processing route for the manufacturing of biomaterials with graded properties.*

Keywords: *β-phase Ti-35Nb-4Sn alloy. Laser welding. Low Young's modulus.*

1. INTRODUCTION

It is known that metallic implants with high elastic modulus can shield the bone from mechanical stresses, which eventually leads to bone resorption, implant loosening and surgery revision (Niinomi and Nakai, 2011). Efforts to minimize stress shielding caused by the elastic modulus mismatch between human bone (10-30GPa) and currently used implant materials, such as the duplex α+β Ti6Al4V (110GPa), resulted in the development of body-centered cubic β- Ti alloys with low elastic modulus, typically below 80 GPa (Niinomi and Nakai, 2011). Ti-35Nb-4Sn (wt%) is among these alloys and has one of the lowest values of Young's modulus reported, about 40 GPa (Niinomi and Nakai, 2011). However, to achieve such low elastic modulus, proper chemical composition and thermomechanical processing is necessary (Guo et al., 2015). Regarding chemical composition, low interstitial levels is necessary, along with Nb additions of about 35wt%, to meta-stabilize Ti-β phase at room temperature (Hon et al., 2003), and Sn additions, to suppress or retard precipitation of the non-compact hexagonal ω phase, that notably increase the elastic modulus. As Sn additions were found to decrease the corrosion resistance (Dalmau et al., 2015; Pina et al., 2015), alloys with smaller tin content are also being studied, such as Ti35Nb and Ti35Nb2Sn (Cremasco et al., 2016). In these other alloys, the elastic modulus is strongly dependent on the thermomechanical processing and can reach up to 110 GPa, after few hours aging due to precipitation of ω and hexagonal close-packed α phases (Cremasco et al., 2016). Regarding thermomechanical processing, solubilization treatment of stiff precipitates (ω and α), followed by quenching and severe cold work must also be performed (Bonisch et al., 2013; Matsumoto et al., 2007). A decrease in elastic modulus of Ti-Nb alloys has been observed for cold rolling reduction over 50% (Matsumoto et al., 2007) and 65% (Hayama et al., 2014) and is usually associated to the formation of strain-induced α"-martensite, with base-centered orthorhombic structure.

Besides alloy design, laser processing has been extensively studied as a tool to improve the performance of biomedical implants (Vilar, 2016). Among these applications are the use of laser surface texturing to improve osteointegration (Pou et al., 2017; Faeda et al., 2009) and laser nitriding to improve wear and corrosion resistance (Chan et al., 2016). Laser processing is also being studied for the manufacturing of components with functionally graded elastic modulus (Lima et al., 2017; Lin et al., 2013; Traini et al, 2018). This is of particular interest in bone plates for fracture healing, in which overall low elastic modulus is desired to minimize stress shielding while local high elastic modulus is necessary to stabilize the fracture site. Tailoring of elastic modulus in Ti-Nb alloys has been achieved by laser additive manufacturing using graded chemical composition (Lin et al., 2013) and by localized aging treatment (Lopes et al., 2015; Jung et al., 2009). However, despite the advantages of laser processing, the imposed thermal cycle induces metallurgical transformations that may cause undesired local change in materials properties (Vilar, 2016). When the material is melted, three characteristic zones can be typically identified: the unaffected base metal, whose original properties remain the same, the heat affected zone (HAZ), where transformations as tempering, recrystallization and grain growth may occur, and the fusion zone, where quenching, phase transformations, dendritic solidification and metallic vaporization can occur, among others. These zones are typically called weld zones. As laser is a high energy density process, weld zones resulting from laser processing can be short-ranged and micro characterization techniques are necessary for precise characterization of each weld zone (Abraham et al., 2015).

In this work, the effect of laser melting in microstructure, mechanical and electrochemical properties of Ti35Nb4Sn alloy is assessed. Microhardness, elastic modulus, and elastic and plastic energy absorption of each weld zone (determined by nanoindentation) are discussed as a function of microstructure and chemical composition. Electrochemical properties are determined using a novel capillary-based microcell setup, in which microcapillary consists in a laser perforated PET (polyethylene terephthalate) mask. Differences in corrosion resistance parameters and pitting susceptibility are discussed as a function of microstructure and chemical composition changes for each weld zone.

2. MATERIALS AND METHODS

A high purity charge of Ti-35Nb-4Sn (wt%) was arc melted under analytical argon atmosphere for at least 10 times. The ingot was cold rolled to a 9 mm thickness, ultrasonically degreased with acetone, encapsulated in a quartz tube under argon atmosphere, homogenized for the 24h at 1000ºC, and water quenched at 0ºC. Homogenized ingot was cold rolled along ten passes from 9 to 3 mm (66% reduction), chemically stripped (1HF: 1HNO3: 5H2O) and ultrasonically cleaned.

A plate sample of about 25×15×3 mm was laser melted at the transverse direction. An Yb-fiber laser with Gaussian beam, M^2 factor of 9, wavelength of 1080 nm, 50 µm of focal beam radius and 160 mm of focal distance was used. Melting was performed with 1000W of power, scan speed of 10 $mm.s^{-1}$ and a defocusing distance of 5 mm. A protective helium flow of 10 $l.min^{-1}$ was provided. The beam radius and power density at the defocused plane were 313 µm and $324kW/cm^2$, respectively.

The cross-section of laser melted track was subjected to metallographic preparation by cold mounting, grinding up to 1200 grit and polishing with 1 and 0.3 µm alumina and 0.04 µm colloidal silica. For microstructure analysis, surface was etched with Kroll solution (3 ml HF, 6 ml HNO_3 and 91ml H_2O). The solidification microstructures were investigated by optical microscopy (OM), scanning electron microscopy (SEM) and electron backscatter diffraction (EBSD), with an indexing rate of 91%. The electron microscopy work has been performed with FEI/THERMO Quanta 650 FEG available at LNNano, Campinas. Phase determination was carried out by X-ray diffraction (XRD) analysis on cross section of base metal and fusion zone. A multi detector equipment with 255 channels, Cu Kα radiation, 40 mA and 40 kV, parallel x-ray lenses and 2×2 mm crossed slits were used. Samples were scanned from 30 to 90º, with a step size of about 0.0131º per channel (active length of 3.3473º), and a step time of 100 s.

The chemical composition of base metal, heat affected zone and fusion zone were analyzed at the cross-section of the weld by energy-dispersive x-ray spectroscopy (EDS), after metallographic preparation, in areas of about 150×150 µm. To investigate possible atmospheric contamination during laser processing, samples of about 100 mg of base metal and weld zone (fusion zone and heat affected zone) were stripped in 1HF: $1HNO_3$: $5H_2O$ solution, ultrasonically cleaned in distilled water and analyzed for oxygen and nitrogen content in LECO TC500 analyzer.

Vickers microhardness mapping of the weld zone was performed on the cross-section of the weld, under 100 gf load, every 100 µm in both longitudinal and transversal directions. Vickers microhardness profile was determined from the center of the weld to the base metal as an average of three rows with 44 indentations each, with a spacing of three times the length of the indentation diagonal. Elastic modulus profile was determined by instrumented nanoindentation and calculated from load-displacement curves, according to the method developed by Oliver and Pharr (2004). Two rows with 19 indentations each were performed from the center of the weld to the base metal. Maximum load of 0.5 gf, pause of 10 s, and loading and unloading rates of 1000 $mN.min^{-1}$ were applied.

The electrochemical response of different weld zones was examined in NaCl solution by linear potential scan voltammetry using an innovative three-electrode microcell. Fig. 1. A pseudo-reference electrode consisting of a tungsten thread with a diameter of 125 µm, oxidized for a hundred cycles in 0.1 $mol.dm^{-3}$ H_2SO_4 solution from 0.954 to 1.854V *vs.* saturated Ag/AgCl, was used (Pasti et al., 2012). This oxidized tungsten electrode is hereafter symbolized by

W/W_xO_y. A platinum thread with diameter of 100 µm was used as the counter electrode. The electrolyte consisted in deaerated saline solution of 0.8% NaCl pH 7.4 (same concentration and pH as simulated body fluid – SBF solution) (Kokubo and Takadama, 2016). The electrolyte volume was a drop of about 30 µL. The open circuit potential (OCP) of the oxidized tungsten electrode *vs.* Ag/AgCl was of -176mV in NaCl electrolyte solutions. The analysis area was of about 0.04 mm^2 (radius of 113 µm), delimited by a laser drilled adhesive PET (Polyethylene terephthalate) mask. All tests were conducted inside a Faraday cage with controlled relative humidity of 72 ± 3%, to minimize electrolyte vaporization. Before every new polarization, specimen was re-polished with 40 nm colloidal silica, for at least 5 min. Specimen was then ultrasonically cleaned with water, washed with isopropyl alcohol, acetone and distilled water, and dried with compressed N_2 flow.

Linear potential scan voltammetry of micro areas within the weld zones was carried from – 0.6 to 0.7 V (*vs.* W/W_xO_y), after 30 min OCP stabilization, with a scan rate of 1 mV/s and acquisition every 0.2 mV. Corrosion potential and current density were determined considering data recorded within Tafel window (with χ^2 test smaller than 10^{-18}). A large area linear potential scan voltammetry comprising all weld zones was performed using the same parameters up to 0.8 mV *vs.* Ag/AgCl, for SEM investigation of pitting location. Before SEM analysis, specimen was etched with Kroll solution.

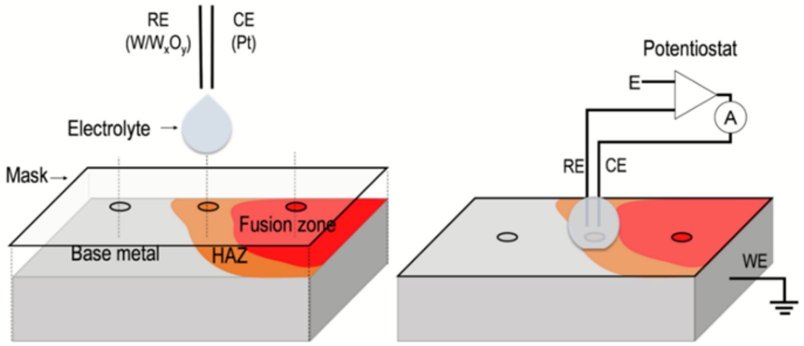

Figure 1. Scheme of the three-electrode microcell set up used in electrochemical characterization of micro areas within the weld zones

3. RESULTS AND DISCUSSION

3.1 Microstructure and Mechanical Properties

Microscopy analysis showed that laser induced significative microstructure changes at the cross-section of the melted track. Fusion zone solidified with a dendritic structure and a keyhole shape, Fig. 2a. A fusion zone with keyhole shape typically forms when a condition of successive laser reflections stablishes at the weld pool walls, increasing energy absorption (Courtois at al., 2013). EBSD band contrast image shown in Fig. 2b clearly shows recrystallization at HAZ and grain growth toward fusion zone. SEM images of the weld zones are shown in Fig. 2c to 2f. Although the microstructure of fusion zone is essentially dendritic, different solidification modes were identified. At fusion boundary, columnar dendritic grains developed following an epitaxial growth from HAZ parent grains, Fig. 2e. As temperature gradient diminished towards the weld centerline, solidification was less directional and resulted in the formation of polygonal grains with equiaxed dendrites, Fig. 2f.

EDS measurements of average chemical composition shown in Table 1 did not accuse any significant difference from one weld zone to another. However, in fusion zone, significant partition of elements occurred within the dendritic structure, Fig. 3. While the dendritic core had higher content of Nb (39.4 wt% ± 0.7) and lower content of Sn (3.8 ± 0.2), the interdendritic region had lower content of Nb (33.1 wt% ± 0.8) and higher content of Sn (4.6 wt% ± 0.1). In non-equilibrium solidification conditions, such as weld bead solidification, the high cooling rates suppress chemical composition homogenization by atomic diffusion. As seen in Ti-Nb phase diagram Zhang et al., 2001), the solidification temperature increases with Nb additions up to 2500 ºC, for pure Nb. On the other hand, Sn additions tend to decrease solidification temperature due to its low melting point 230ºC. This way, it is coherent that, under fast cooling, clusters with high Nb and low Sn content would solidify first, serving as nuclei for dendrites growth. At the same time, the remaining liquid with low Nb and high Sn content would solidify last, at the interdendritic region.

Besides Nb and Sn partition, another difference in chemical composition of fusion zone was observed. Interstitial analysis showed that, from base metal to weld zone, oxygen content increased from 0,158% to 0,179% while nitrogen content nearly doubled, from 0,068% to 0,122%. The increase in interstitial content might have been caused by insufficient shielding of the melting pool against atmospheric contaminations, during laser processing. The distribution of these interstitials in the weld zone could not be resolved by EDS, as their content is below the minimum required for reliable detection.

Table 1 – Average chemical composition of the alloy determined by EDS in different weld zones (wt%)

Ti	**Nb**	**Sn**
59.4 ± 0.1	36.4 ± 0.2	4.2 ± 0.1

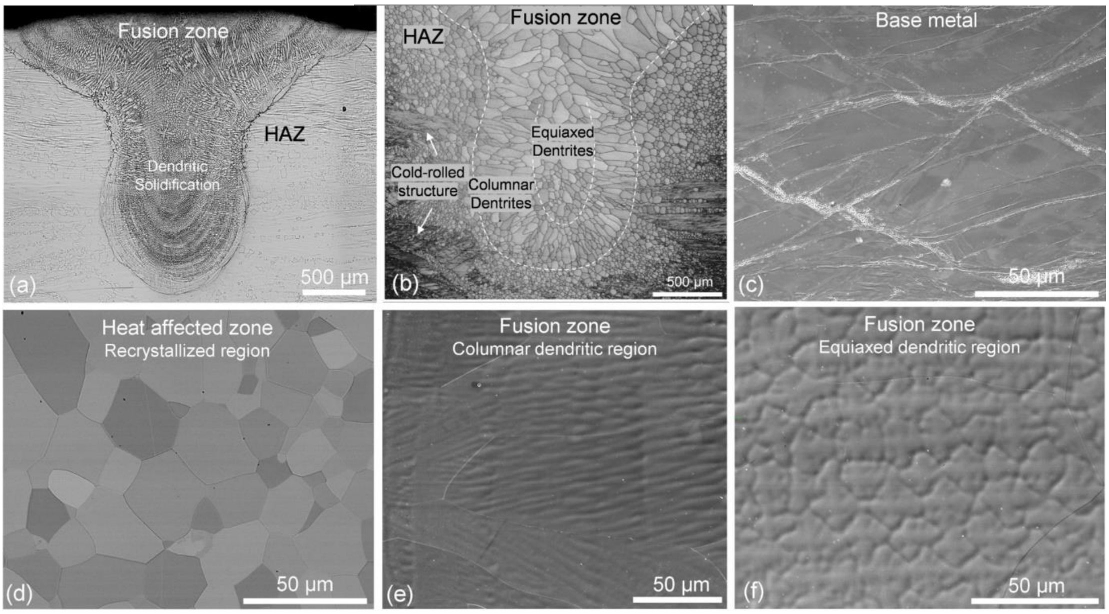

Figure 2. Microstructure of laser processed Ti35Nb4Sn alloy: (a) optical microscopy of weld cross-section showing dendritic solidification and the keyhole shape of the melted track. (b) EBSD band contrast image showing recrystallization and grain growth from base metal toward fusion zone. Dashed-line of (b) roughly separates microstructure of weld zones. SEM images of (c) cold-rolled base metal, (d) recrystallized HAZ, (e) columnar dendritic solidification at fusion zone boundary and (f) equiaxed dendritic solidification at fusion zone centerline

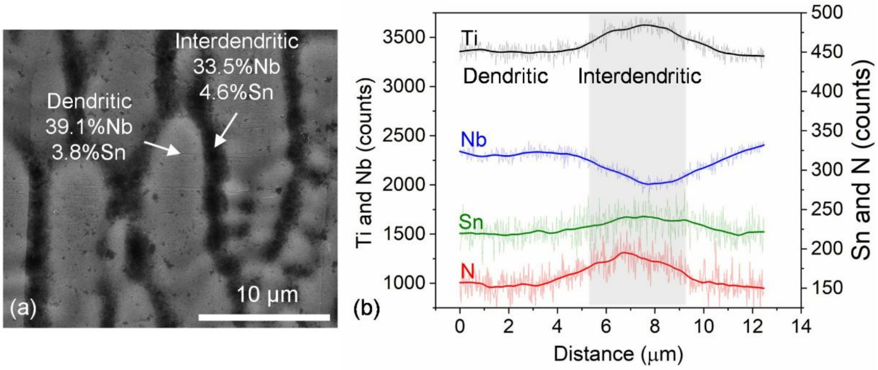

Figure 3. EDS Chemical composition across dendrites in fusion zone, revealing dendritic core enriched with Nb. Sn content is 0.8wt% higher at interdendritic region

The increase in interstitials content had important implications in mechanical properties of fusion zone. Fig. 4a shows the 3D microhardness maps of keyhole cross-section, where great increase in hardness occurred, despite the expected reduction in hardness due to recrystallization and grain growth, shown in Fig. 2b, XRD analysis at Fig. 5 reveals that this abrupt increase in microhardness is not associated with phase transformations, as both base metal and fusion zone regions presented β-structure. While microhardness of polygonal equiaxed dendritic grains, found in central regions of the keyhole, ranged from about 270 HV to 330 HV, microhardness at fusion boundaries reached a maximum of 396 HV. EDSD analysis provided evidence that the higher microhardness at fusion boundaries are related to higher degree of lattice distortions at this zone. Fig. 4b shows EBSD band slope image of the keyhole, where regions with poorer crystallinity are darker than those with higher crystallinity. Although crystallinity of fusion zone and HAZ is partially improved with recrystallization, significant lattice distortion can be seen along fusion boundary. These results are in full agreement with those reported by Turner et al. (2016), in which residual stresses induced by the solidification of a keyhole laser weld are higher in fusion zone than in HAZ or base metal and are maximum at the very edge of the weld bead. Therefore, the higher content of interstitials seems to be a primary cause for the abrupt increase in microhardness of fusion zone, while the higher concentration of lattice distortions is a secondary cause. Together, these two factors account for the broadening of XRD peaks from base metal to fusion zone regions, as observed by the increase in full width at half maximum (FWHM) measurements shown in Fig. 5. The correlation of diffraction line broadening and lattice parameters distortions is well stablished (Balzar, 1996) and has been used to assess the performance of welds (Jun et al., 2012).

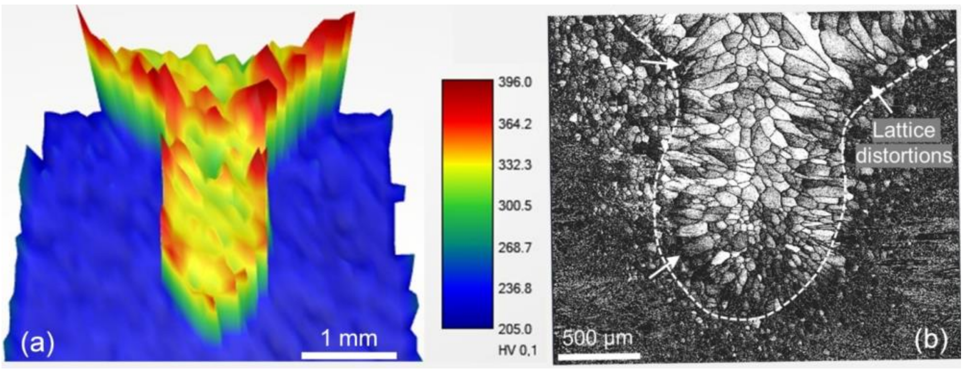

Figure 4. (a) 3D microhardness maps on keyhole cross-section showing abrupt increase in microhardness of fusion zone, in comparison to base metal and heat affected zone, especially at fusion boundaries. (b) EBSD band slope image on keyhole cross-section showing darker regions on fusion zone boundaries with higher lattice distortion

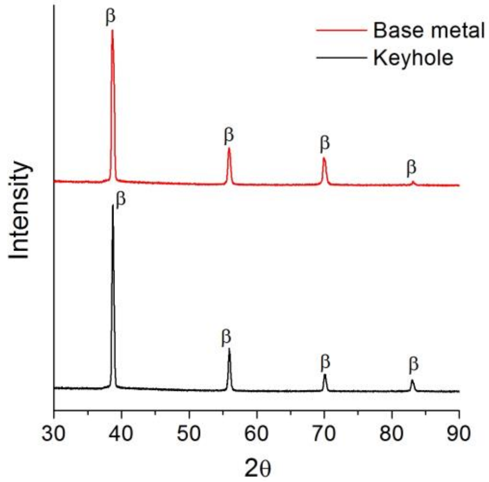

Figure 5. XRD analysis of base metal and fusion zone regions showing no phase transformations with laser melting

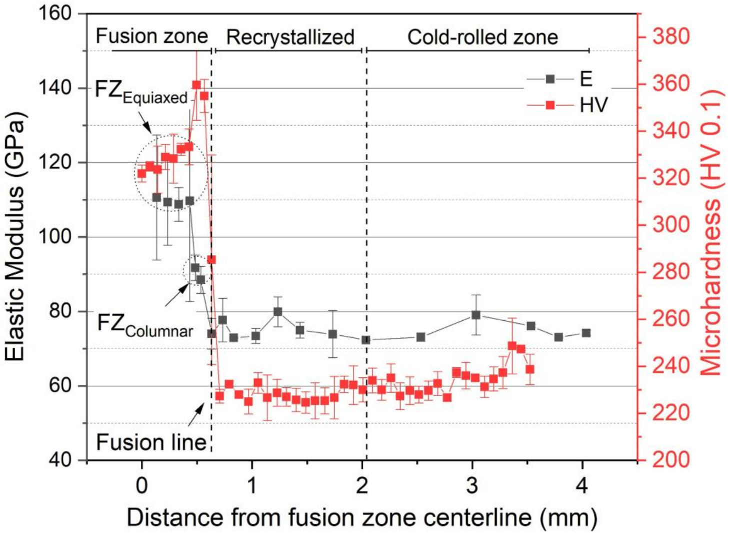

Figure 6. Elastic modulus and microhardness profile from fusion zone centerline to base metal. Hardness decreased at heat affected zone due to recrystallization. Hardness and elastic modulus increased at fusion zone due to higher interstitial content

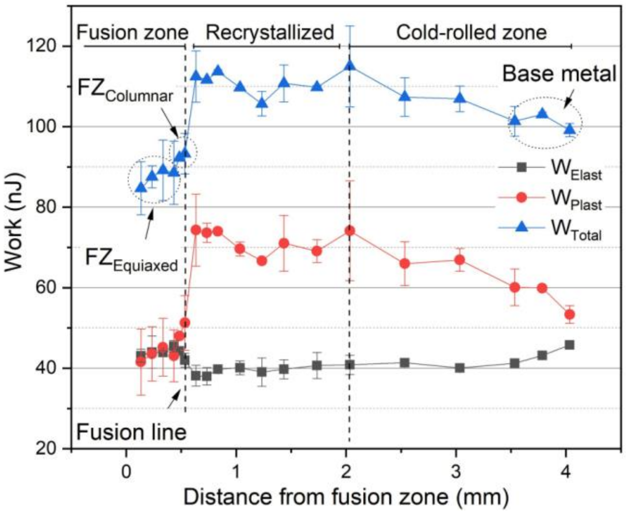

Figure 7. Elastic, plastic and total work on the melted profile. Increase in plastic and decrease in elastic energy absorption of HAZ with annealing and recrystallization. Decrease in plastic and increase in elastic energy absorption of fusion zone with increase in interstitials content

Fig. 6 shows the elastic modulus and microhardness profile from fusion zone to cold-rolled base metal. Recrystallization promoted a gradual decrease in microhardness from base metal toward HAZ but had no significant effect on the elastic modulus. This shows that no further reduction in elastic modulus was obtained with the 66% reduction cold-rolling. Although progressive decrease in elastic modulus could be expected for rolling reductions over 50% (Matsumoto et al., 2007), maximum reductions were only achieved after severe plastic deformation (~90% rolling reduction) (Guo et al., 2015; Matsumoto et al., 2007). As elastic modulus reduction is usually associated to the formation of strain induced α”-martensite, this result is coherent with XRD measurements that did not accuse its presence in the cold-rolled base metal, Fig. 5. While both interstitial content and lattice distortions affect microhardness, elastic modulus is little affected by dislocation densities, but strongly affected by interstitials content. In β-Ti alloys, elastic modulus is most notably increased by nitrogen (Carquigny et al., 2019) than by oxygen additions (Tane et al., 2016). In α+β alloys, however, oxygen seems to have a more significant effect (Lee and Welsch, 1990). Curiously, the elastic modulus was smaller at fusion boundaries than at fusion zone centerline. This can be associated to the faster solidification of fusion boundaries from the pre-existing solid interface (HAZ), followed by the diffusion of interstitials to the remaining liquid in fusion zone center line, that solidifies last (Kou, 2002).

Fig. 8 shows elastic, plastic and total energy absorption profile of the melted track. In comparison to base metal, total energy absorption of HAZ increased in about 10% while that of fusion zone was reduced in about 14%, as result of differences in plastic and elastic energy absorption of each zone. In fusion zone and base metal, plastic deformation was restrained by the presence of interstitials elements and of abundant dislocations generated by work-hardening, respectively. This accounted for a reduction in plastic energy absorption, that was about 25% smaller in fusion zone than in base metal. On the other hand, recrystallization allowed HAZ to recover its ductility. Maximum plastic energy absorption was found in this region, that was improved in about 24% in comparison to base metal. Progressive increase in toughness from base metal toward the recrystallized zone indicates that some annealing occurred within the cold-rolled region. This annealed zone can also be considered as part of HAZ. Interestingly, recrystallization softening reduced the elastic energy absorption of HAZ in about 9%, in comparison to base metal. In fusion zone, this was compensated by interstitial strengthening and elastic energy absorption was reestablished. Rather than compromising the resilience of the alloy, studies show that additions of nitrogen and oxygen can increase the critical stress for slip and improve the shape memory effect and the superelasticity of Ti-Nb alloys (Tahara etal., 2009; Ataollahi Oshkour et al., 2014). The shape memory effect of Ti-Nb alloys requires specific thermomechanical processing and was not explored in this present study.

Results show that the selected laser processing parameters allowed the formation of a structure with functionally graded elastic modulus, ranging from a relatively low value of 75 GPa up to 110 GPa, which is close to the elastic modulus of currently used implant materials (Niinomi and Nakai, 2011). The development of Ti-Nb implants with graded elastic modulus has been investigated by several researchers (Lima et al., 2017; Lin et al., 2013; Lopes at al., 2015; Jung et al., 2009; Ataollahi Oshkour et al, 2014; Ganesh et al., 2005). Recently, Lima et al. (2017) have used laser additive manufacturing using different chemical compositions to manufacture bone plates with graded elastic modulus from 70GPa to 115GPa, where hardness ranged from 270 to 350 HV. Also, Lopes et al. (2015) have produced a graded elastic modulus femoral hip stem using localized aging by electro-magnetic induction heating, where elastic modulus ranged from 65 GPa to 110 GPa and micro hardness from 225 HV to 420 HV. In this context, laser melting with controlled additions of oxygen or nitrogen stands out as a potential route for manufacturing of components with graded elastic modulus in a fast and simple way.

3.2 Electrochemical Response

Fig. 8 shows open circuit potential and polarization curves of weld regions in NaCl physiological solution. Table 2 summarizes results from Tafel analysis of polarization curves. The shift in OCP curves toward more positive values in Fig. 8a shows that the weld zones undergo spontaneous passivation in the electrolyte solution.

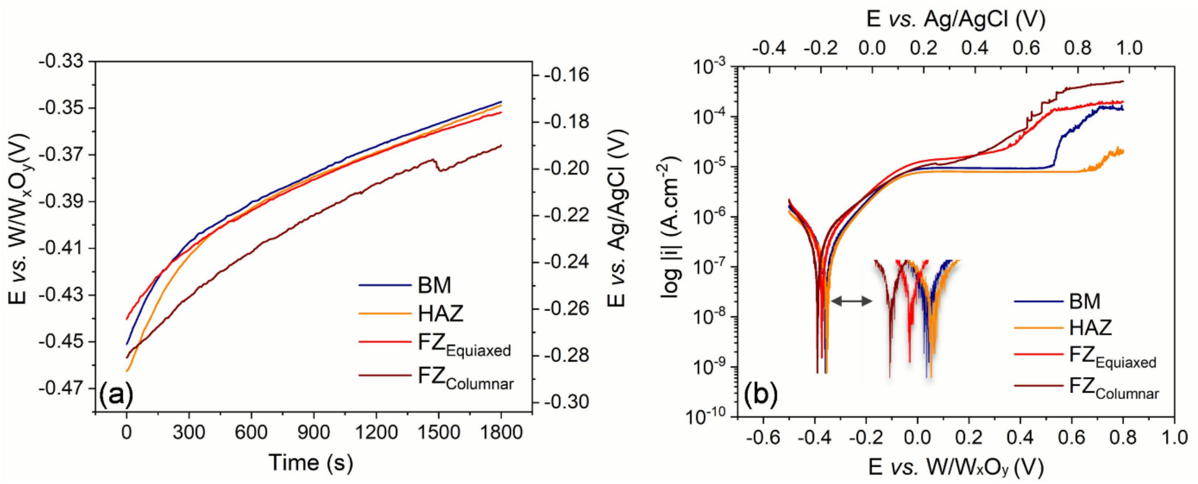

Figure 8. (a) Open circuit potential showing spontaneous passivation of all weld zones in physiological saline solution. (b) Polarization curves showing that passivation is more effective in HAZ and BM and that fusion zone is more anodic and more susceptible to pitting

Table 2 – Parameters adjusted from Tafel region: Corrosion potential E_{corr}, corrosion current density i_{corr}, polarization resistance R_p, pitting potential E_{pit} and passive current dendity i_{pass}

	E_{corr}* (mV)	i_{corr} (μA cm^{-2})	R_p (kΩ cm^2)	E_{pit}*(mV)	i_{pass} (μA cm^{-2})
BM	-358 (-182)	43	121	530 (706)	9.3
HAZ	-355 (-179)	32	148	695 (871)	7.9
FZ$_{Equiaxed}$	-374 (-198)	46	97	—	—
FZ$_{Columnar}$	-390 (-214)	55	92	—	—

**vs.* W/W$_x$O$_y$ (*vs.* Ag/AgCl)

Results show that both equiaxed and columnar regions of fusion zone are the least resistant to polarization. Table 2 shows that fusion zone is anodic in comparison to base metal and HAZ, and that potential difference between the adjacent HAZ and the fusion boundary (FZ columnar) reaches up to 35mV. Besides, fusion zone also presents lower polarization resistances and higher corrosion current densities. On the other hand, both base metal and HAZ presented higher corrosion resistant with more positive corrosion potential and broad passivation plateaus. The difference in the performance of BM and HAZ seems to be related to the surface activity intrinsic of each microstructure. In comparison to the recrystallized structure, the cold-rolled structure has dislocations and other imperfections that increase its free-energy (Rios et al., 2005), and account for a higher surface activity. This facilitates the occurrence of surface reactions and may be the cause for the higher current densities of the cold-rolled structure. Furthermore, the cold-rolled structure of base metal also has more active sites that facilitate pitting nucleation, causing a reduction in pitting potential. Therefore, the lower current densities and higher pitting potential of HAZ are associated to its effective passivation under anodic polarization and to its lower surface activity, that delay surface reactions and pitting nucleation. Regarding the performance of fusion zone, one of the reasons for its inferior corrosion resistance in the higher content of Sn in the interdendritic regions. It has been reported that the increase in Sn content in Ti-Nb-Sn alloys is followed by an increase the dissolution rate of the passive film (Dalmau et al., 2015; Pina et al., 2015) that is proportional to the applied potential and is critical above 4wt% (Dalmau et al., 2015; Pina et al., 2015). Another factor that can account for the decrease in corrosion resistance of fusion zone is the coarse-grained microstructure (Ralton and Birbilis, 2010). A review from Ralston and Birbilis (2010) on the impact of grain sizes on corrosion properties observed that, when the media promotes passivation, grain refinement increases corrosion resistance while grain coarsening reduces it. This is associated to the formation of a more compact passive layer upon the refined structure and a more open passive layer upon the coarse-grained microstructure, as illustrated by Gollapudi (2012). This is coherent with SEM analysis of pitting location, that indicated the occurrence of multiple pitting in fusion zone, preferentially at Sn enriched interdendritic regions, Fig. 9b and c. Elongated pitting at base metal and HAZ can be associated to chemical composition inhomogeneities, aligned during cold rolling. Unlike Sn, Nb content is not critical. Studies on the corrosion resistance of Ti-20Nb and Ti40Nb alloys in NaCl physiological solutions showed that both alloys presented similar corrosion potentials and that Ti-40Nb had higher stability and pitting resistance (Choe et al., 2006). This could be rather related to the more refined and active structure of Ti-20Nb alloy, that is martensitic, than to Nb content itself. As β-phase remained stable even in interdendritic region with lower content of Nb, Nb fluctuations (~32-40wt%) are not expected to have any detrimental effect in the corrosion resistance. Similarly, studies on ion implantation of O (Ningshen et al., 2008), N (Vlcak et al., 2019) and laser surface nitriding (Chan et al., 2016) suggest that alloying with these elements can improve corrosion resistance of Ti alloys, by shifting the corrosion potential to more positive values and by decreasing corrosion current density. Although the higher content of interstitial alone could not improve the corrosion resistance of fusion zone in comparison to BM and HAZ, due to the detrimental effects of Sn fluctuations and grain coarsening, it might have caused the higher corrosion potential of equiaxed dendritic region, in comparison to columnar dendritic region. As discussed before, the higher elastic modulus of equiaxed dendritic region may be associated to diffusion of interstitials to this region during solidification.

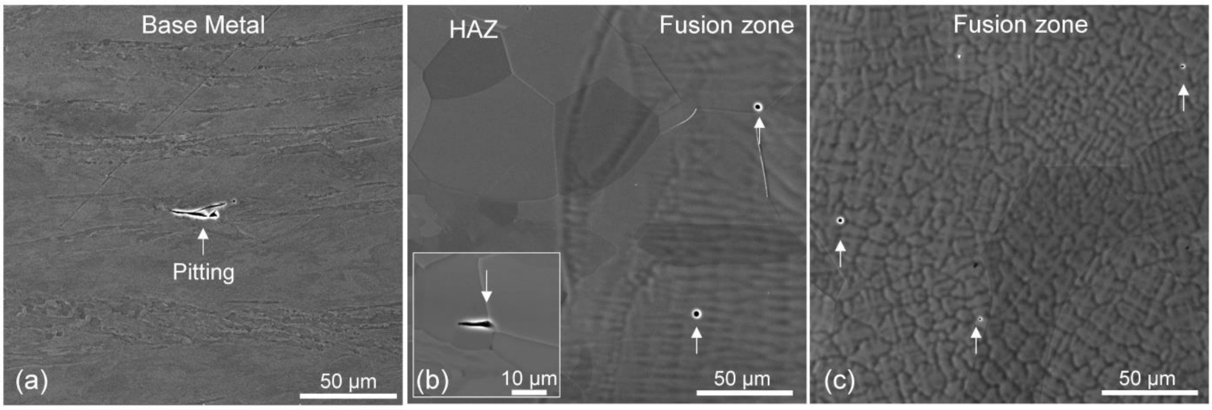

Figure 9. Pitting morphology and location after simultaneous anodic polarization of all weld zones up to 0.8mV vs. Ag/AgCl. Elongated pitting in (a) base metal and (b) HAZ, and multiple pitting corrosion in (b) fusion boundary and fusion zone, with preferential pitting at Sn enriched interdendritic regions

4. CONCLUSIONS

Fiber laser melting was performed on top of a 3 mm-thick β-type Ti-35Nb-4Sn alloy. Microstructure changes as well as mechanical and electrochemical responses in NaCl physiological solution were assessed. The main conclusions are presented as follows:

Laser melting did not cause any phase transformation in the initial β structure, but induced recrystallization at heat affected zone. This did not affect the elastic modulus of HAZ, but slightly reduced the microhardness and the elastic energy absorption. On the other hand, recrystallization greatly increased plastic energy absorption in about 25%, in comparison to base metal. HAZ presented clear passivation plateau and higher pitting potential than base metal, whose cold-rolled microstructure provided more active sites for pitting nucleation.

Laser melting induced recrystallization and grain coarsening at fusion zone. This region also presented a dendritic structure, where Nb partitioned to dendritic core and Sn partitioned to interdendritic region.

Laser processing also induced an increase in the content of oxygen and nitrogen of fusion zone which locally increased microhardness, from about 200 HV to 330 HV, and the elastic modulus, from 75GPa to 110GPa. Fusion boundaries developed higher lattice distortions which contributed for further increase in microhardness up to about 400 HV and resulted in an intermediate elastic modulus of 90 GPa. Elastic energy absorption of fusion zone was sustained, but plastic energy absorption was reduced.

The electrochemical performance and passivation of fusion zone was impaired by the higher content of Sn in interdendritic region and by its coarser microstructure. Fusion zone was the most anodic region. Under anodic polarization, it presented a corrosion potential difference of 35mV, in comparison to the adjacent and most cathodic HAZ. Unlike base metal and HAZ, fusion zone did not present a clear passivation plateau and was more susceptible to pitting corrosion, that occurred preferentially at Sn enriched interdendritic regions.

5. ACKNOWLEDGEMENTS

The authors would like to thank FAPESP for research founding Proc. FAPESP 2016/10637-4, CAPES for graduation scholarship, and the LNNano/CNPEM/MCTIC for technical support during electron microscopy work. Special thanks to Dr. Getúlio de Vasconcelos and MSc. Renê Volu for their support with laser drilling, to Eng. Vitor Ribeiro for his support with instrumented nanoindentation analysis, to Dr. Victor Riguetti for his support with x-ray diffraction analysis and to Dr. Vinicius Henriques for his support with interstitials content analysis.

6. REFERENCES

Niinomi, M., Nakai, M., 2011. “Titanium-Based Biomaterials for Preventing Stress Shielding between Implant Devices and Bone”. *International Journal of Biomaterials*. Pp. 1–10.

Guo, S., Meng, Q., Zhao, X., Wei, Q., Xu, H., 2015. “Design and fabrication of a metastable β-type titanium alloy with ultralow elastic modulus and high strength”. *Scientific Reports*. Vol. 5, pp. 1-8.

Hon, Y.-H., Wang, J.-Y., Pan, Y.-N., 2003. “Composition/Phase Structure and Properties of Titanium-Niobium Alloys”. *Materials Transactions*. Vol. 44, No. 11, 2384–2390.

Dalmau, A., Pina, V. G., Devesa, F., Amigó, V., Muñoz, A. I., 2015. “Electrochemical behavior of near-beta titanium biomedical alloys in phosphate buffer saline solution”. *Materials Science and Engineering: C*. Vol. 48, pp. 55–62.

Pina, V. G., Dalmau, A., Devesa, F., Amigó, V., Muñoz, A. I., 2001. “Tribocorrosion behavior of beta titanium biomedical alloys in phosphate buffer saline solution. *Journal of the Mechanical Behavior of Biomedical Materials*”. Vol. 46, pp. 59–68.

Cremasco, A., Lopes, E. S. N., Bertazzoli, R., Caram, R., 2016. “Application of coupled substrate aging and TiO2 nanotube crystallization heat treatments in cold-rolled Ti–Nb–Sn alloys”. *Journal of Materials Science*. Vol. 51, No. 13, pp. 6389–6399.

Bönisch, M., Calin, M., Waitz, T., Panigrahi, A., Zehetbauer, M., Gebert, A., 2013. “Thermal stability and phase transformations of martensitic Ti–Nb alloys”. *Science and Technology of Advanced Materials*. Vol. 14, No. 5, pp. 55004.

Matsumoto, H., Watanabe, S., Hanada, S., 2007. “Microstructures and mechanical properties of metastable β TiNbSn alloys cold rolled and heat treated”. *Journal of Alloys and Compounds*. Vol. 439, No. 1–2, pp. 146–155.

Hayama, A. O. F., Lopes, J. F. S. C., Gomes da Silva, M. J., Abreu, H. F. G., Caram, R., 2014. “Crystallographic texture evolution in Ti–35Nb alloy deformed by cold rolling”. *Materials & Design*. Vol. 60, pp. 653–660.

Vilar, R., 2016. *Laser Surface Modification of Biomaterials*. Elsevier; 2016.

Pou, P., Riveiro, A., del Val, J., Comesaña, R., Penide, J., Arias-González, F., 2017. “Laser surface texturing of Titanium for bioengineering applications”. *Procedia Manufacturing*. Vol. 13, pp. 694–701.

Faeda, R.S., Tavares, H.S., Sartori, R., Guastaldi, A.C., Marcantonio, Jr. E., 2009. “Evaluation of titanium implants with surface modification by laser beam: biomechanical study in rabbit tibias”. *Brazilian Oral Research*. Vol. 23, No. 2, pp. 137–143.

Chan, C.-W., Lee, S., Smith, G., Sarri, G., Ng, C.-H., Sharba, A., et al., 2016. Enhancement of wear and corrosion resistance of beta titanium alloy by laser gas alloying with nitrogen. *Applied Surface Science*. Vol. 367,pp. 80–90.

Lima, D. D., Mantri, S.A., Mikler, C. V., Contieri, R., Yannetta, C. J., Campo, K. N., et al., 2017. “Laser additive processing of a functionally graded internal fracture fixation plate”. *Materials & Design*. Vol. 130, pp. 8–15.

Lin, W.-S., Starr, T. L., Harris, B. T., Zandinejad, A., Morton, D., 2013. “Additive Manufacturing Technology as a Novel Approach to Fabricate Functionally Graded Titanium Implants: Preliminary Investigation of Fabrication Parameters”. *The International Journal of Oral & Maxillofacial Implants*. Vol. 28, No 6, pp. 1490–1495.

Traini, T., Mangano, C., Sammons, R.L., Mangano, F., Macchi, A., Piattelli, A., 2008. “Direct laser metal sintering as a new approach to fabrication of an isoelastic functionally graded material for manufacture of porous titanium dental implants”. *Dental Materials*. Vol. 24, No. 11, pp. 1525–33.

Lopes, E. S. N., Contieri, R. J., Button, S. T., Caram, R., 2015. “Femoral hip stem prosthesis made of graded elastic modulus metastable β Ti Alloy”. *Materials & Design*. Vol. 69, pp. 30–36.

Jung, T. K., Matsumoto, H., Abumiya, T., Masahashi, N., Kim, M. S., Hanada, S., 2010. “Mechanical Properties-Graded Ti Alloy Implants for Orthopedic Applications”. *Materials Science Forum*. Vol. 631–632, pp. 205–10.

Abraham, G. J., Kain, V., Dey, G. K., Raja, V. S., 2015. “Corrosion characterization of laser beam and tungsten inert gas weldment of nickel base alloys: Micro-cell technique”. *Corrosion Science*. Vol.93, pp.1–8.

Oliver, W. C., Pharr, G. M., 2004. “Measurement of hardness and elastic modulus by instrumented indentation: Advances in understanding and refinements to methodology”. *Journal of Materials Research*. http://dx.doi.org/10.1557/jmr.2004.19.1.3 Vol.19, No. 1, pp. 3-20.

Pašti, I. A., Lazarević-Pašti, T., Mentus, S. V., 2012. “Switching between voltammetry and potentiometry in order to determine H+ or OH− ion concentration over the entire pH scale by means of tungsten disk electrode”. *Journal of Electroanalytical Chemistry*. Vol. 665, pp. 83–89.

Kokubo, T. and Takadama, H., 2016. “How useful is SBF in predicting in vivo bone bioactivity?”. *Biomaterials*. Vol. 27, No. 15, pp. 2907–15.

Courtois,M., Carin, M., Le Masson, P., Gaied, S., 2013. “A two-dimensional axially-symmetric model of keyhole and melt pool dynamics during spot laser welding”. *Revue de Métallurgie*. Vol. 110, No. 2. pp. 165–73.

Zhang, Y., Liu, H., Jin, Z., 2001. “Thermodynamic assessment of the Nb-Ti system”. *Calphad*. Vol. 25, No. 2, pp. 305–17.

Turner, R. P., Panwisawas, C., Sovani, Y., Perumal, B., Ward, R. M., Brooks, J. W., et al., 2016. “An Integrated Modeling Approach for Predicting Process Maps of Residual Stress and Distortion in a Laser Weld: A Combined CFD–FE Methodology”. *Metallurgical and Materials Transactions B*. Vol. 47, No 5, pp. 2954–62.

Balzar, D., 1996. “Diffraction line broadening - Nuisance or lattice-imperfections fingerprints”, *Croat. Chem. Acta*. Vol. 69, pp. 1069–1115.

Jun, T.-S., Hofmann, F., Hofmann, M., Korsunsky, A. M., 2012. “Residual stress characterization in 12%-Cr steel friction stir welds by neutron diffraction”. *The Journal of Strain Analysis for Engineering Design*. Vol. 47, No. 4, pp. 203–13.

Carquigny, S., Takadoum, J., Ivanescu, S., 2019. “Comparative study of nitrogen implantation effect on mechanical and tribological properties of Ti-6Al-4V and Ti-10Zr-10Nb-5Ta alloys”. *The European Physical Journal Applied Physics*. Vol. 85, No. 2, pp. 21301.

Tane, M., Hagihara, K., Ueda, M., Nakano, T., Okuda, Y., 2016. “Elastic-modulus enhancement during room-temperature aging and its suppression in metastable Ti–Nb-Based alloys with low body-centered cubic phase stability”. *Acta Materialia*.Vol. 102, pp. 373–84.

Lee, Y. T. and Welsch, G., 1990. “Young’s modulus and damping of Ti-6Al-4V alloy as a function of heat treatment and oxygen concentration”. *Materials Science and Engineering: A*. Vol. 128, No. 1, pp. 77–89.

Kou, S., 2002. *Welding Metallurgy*. John Wiley & Sons, Inc., Hoboken, New Jersey.

Kim, J. I., Kim, H. Y., Hosoda, H., Miyazaki, S., 2005. “Shape Memory Behavior of Ti–22Nb–(0.5–2.0)O(at%) Biomedical Alloys”. *Materials Transactions*. Vol. 46, No. 4, pp. 852–857.

Tahara, M., Kim, H., Hosoda, H., Miyazaki, S., 2009. “Shape Memory Effect and Cyclic Deformation Behavior Of Ti–Nb–N Alloys”. *Functional Materials Letters*. Vol. 2, No. 2, pp. 79–82.

Ataollahi Oshkour, A., Talebi, H., Seyed Shirazi, S.F., Bayat, M., Yau, Y.H., Tarlochan, F., et al., 2014. “Comparison of Various Functionally Graded Femoral Prostheses by Finite Element Analysis”. *The Scientific World Journal*. Vol. 227 , No.1 , pp. 3-17.

Ganesh, V., Ramakrishna, K., Ghista, D. N., 2005. “Biomechanics of bone-fracture fixation by stiffness-graded plates in comparison with stainless-steel plates”. *BioMedical Engineering OnLine*. Vol. 4, No. 1, pp. 46

Rios, P.R., Siciliano, Jr. F., Sandim, H.R.Z., Plaut, R.L., Padilha, A.F., 2005. “Nucleation and growth during recrystallization”. *Materials Research*. Vol. 8, No. 3, pp. 225–238.

Ralston, K.D. and Birbilis, N., 2010. “Effect of Grain Size on Corrosion: A Review”. *Corrosion*. Vol. 66, No. 7, pp. 75005-075005–13.

Gollapudi, S., 2012. “Grain size distribution effects on the corrosion behaviour of materials”. *Corrosion Science*. Vol. 32, pp.90–4.

Choe, H.-C., Ko, Y.-M., Park, H.-O., 2006. “Electrochemical behavior of TiN film coated Ti–Nb alloys for dental materials”. *Metals and Materials International*. Vol. 12, No. 4, pp. 365–369.

Ningshen, S., Kamachi, Mudali. U., Mukherjee, P., Sarkar, A., Barat, P., Padhy, N., et al., 2008. “Influence of oxygen ion irradiation on the corrosion aspects of Ti-5%Ta-2%Nb alloy and oxide coated titanium”. *Corrosion Science*. Vol.50, No.8, pp. 2124–2134.

Vlcak, P., Fojt, J., Weiss, Z., Kopeček, J., Perina, V., 2019. “The effect of nitrogen saturation on the corrosion behaviour of Ti-35Nb-7Zr-5Ta beta titanium alloy nitrided by ion implantation”. *Surface and Coatings Technology*.Vol. 358, pp.144–152.

7. RESPONSIBILITY NOTICE

The authors are the only responsible for the printed material included in this paper.